


Cite this: *Nanoscale Adv.*, 2021, 3, 4961

# The effect of PEGylation on the efficacy and uptake of an immunostimulatory nanoparticle in the tumor immune microenvironment

Wyatt M. Becicka,<sup>†a</sup> Peter A. Bielecki,<sup>†ab</sup> Morgan E. Lorkowski,<sup>†a</sup> Taylor J. Moon,<sup>a</sup> Yahan Zhang,<sup>a</sup> Prabhani U. Atukorale,<sup>ab</sup> Gil Covarrubias<sup>ab</sup> and Efstathios Karathanasis <sup>\*ab</sup>

The efficacy of immunotherapies is often limited by the immunosuppressive tumor microenvironment, which is populated with dysfunctional innate immune cells. To reprogram the tumor-resident innate immune cells, we developed immunostimulatory silica mesoporous nanoparticles (immuno-MSN). The cargo of immuno-MSN is a Stimulator of Interferon Gene (STING) agonist, which activates innate immune cells leading to production of interferon (IFN)  $\beta$ . By proficiently trafficking its cargo into immune cells, the immuno-MSN induced a 9-fold increase of IFN- $\beta$  secretion compared to free agonist. While an external PEG shield has historically been used to protect nanoparticles from immune recognition, a PEGylated immunostimulatory nanoparticle needs to strike a balance between immune evasion to avoid off-site accumulation and uptake by target immune cells in tumors. Using the 4T1 mouse model of metastatic breast cancer and flow cytometry, it was determined that the degree of PEGylation significantly influenced the uptake of 'empty' MSNs by tumor-resident innate immune cells. This was not the case for the agonist-loaded immuno-MSN variants. It should be noted the surface charge of the 'empty' MSNs was positive rather than neutral for the agonist-loaded immuno-MSNs. However, even though the cellular uptake was similar at 24 h after injection for the three immuno-MSN variants, we observed a significant beneficial effect on the activation and expansion of APCs especially in lung metastasis using the lightly PEGylated immuno-MSN variant.

Received 26th April 2021  
Accepted 23rd July 2021DOI: 10.1039/d1na00308a  
[rsc.li/nanoscale-advances](https://rsc.li/nanoscale-advances)

## 1. Introduction

One of the major hurdles in cancer immunotherapies is to overcome a highly immunosuppressive tumor microenvironment.<sup>1–3</sup> These immunologically “cold” tumors are populated with highly immunosuppressive and dysfunctional immune cells that shield the tumor from the infiltration of systemic effector immune cells.<sup>4,5</sup> Specifically, the tumor's perivascular regions become populated with a large concentration of dysfunctional innate immune cells, such as M2-like tumor associated macrophages (TAMs) and dendritic cells (DCs). When these cells are properly functioning, they serve as vital antigen-presenting cells (APCs) for creating a functional T cell response.<sup>5–8</sup> Without reversing the immunosuppressive innate immune compartment, a tumor remains immune-privileged, with a strong chemical gradient that discourages an anti-tumor response from the host immune system.

To address the issue of local immunosuppression, pro-inflammatory immunomodulatory drugs can reprogram the dysfunctional APCs into properly activated immune cells, which can then bridge the innate and adaptive compartments of the immune system.<sup>9–11</sup> A family of potent immunomodulatory agents consist of cyclic dinucleotides (CDNs) that serve as Stimulator of Interferon Gene (STING) agonists. Activation of the STING pathway triggers the body's natural response to foreign DNA through secretion of interferon  $\beta$  (IFN- $\beta$ ), leading to activation of dendritic cells, macrophages and natural killer cells.<sup>12–14</sup> Considering the nature of nucleotides, nanoparticles can address a number of drug delivery challenges that CDNs face, including off-site toxicity, degradation in blood circulation, and limited penetration across the cell membrane. Further, systemic administration of nanoparticles loaded with immunomodulatory drugs such as STING agonists offers many advantages, including convenient access to the entire tumor volume using the tumor microvasculature, preferential deposition within the tumor's perivascular niche that coincides with the APC-rich regions, and effective delivery to sites of early metastatic spread throughout the body.<sup>12,15–21</sup>

We designed an immunostimulatory nanoparticle loaded with a STING agonist (*i.e.*, CDN) using mesoporous silica

<sup>a</sup>Department of Biomedical Engineering, Case Western Reserve University, Cleveland, OH, USA. E-mail: [stathis@case.edu](mailto:stathis@case.edu)<sup>b</sup>Case Comprehensive Cancer Center, Case Western Reserve University, Cleveland, OH, USA<sup>†</sup> Equal contribution.

nanoparticles (termed immuno-MSNs).<sup>19</sup> The immuno-MSN provides an extremely high specific surface area, enabling a high drug-to-excipient ratio.<sup>22,23</sup> Additionally, the mesoporous structure of MSNs can be readily functionalized with positively charged amines that can tightly bind the negative phosphonate groups of CDN. We used ethylene triamine, which is a small molecule with three amines in close proximity, giving these amines a  $pK_a$  in the desirable range of 6–7.<sup>24</sup> Due to the high content of amines with the appropriate  $pK_a$ , the immuno-MSN facilitates efficient intracellular delivery of CDN due to endosomal escape of the nanoparticle *via* the proton sponge effect.<sup>19,25</sup> In a recent study,<sup>19</sup> we showed the immuno-MSN exhibited stable loading of the STING agonist, protection of its cargo in blood circulation, enhanced delivery and uptake by the dysfunctional tumor-resident APCs, and proficient intracellular presentation of the immune agonist leading to reprogramming and activation of the innate arm of the immune system in a tumor.

The purpose of this study was to assess the effect of polyethylene glycol (PEG) on the microdistribution and cell uptake of immuno-MSNs. In the context of traditional drug delivery, PEGylation has historically been used on the surface of nanoparticles to evade immunosurveillance.<sup>26–28</sup> The presence of an inert, hydrophilic polymer on the particle surface sterically decelerates non-specific protein adsorption that would otherwise lead to increased immunogenicity of the nanoparticle and accelerated uptake by immune cells. In the case of immunostimulatory nanoparticles, however, a balance needs to be struck between immune evasion to avoid off-site uptake and associated toxicity and uptake by target immune cells. Considering the complex network of feedback between immune cells, we sought to determine the influence of the degree of PEGylation and PEG conformation on the uptake of immuno-MSNs by different immune cell subtypes within the microenvironment of primary tumor and early metastasis.

## 2. Experimental section

### 2.1 Synthesis of nanoparticles

The immuno-MSNs were synthesized using an established method.<sup>19</sup> Briefly, 5.7 mL of a 25% (wt/wt) aqueous cetyltrimethylammonium bromide (CTAB, Sigma-Aldrich) solution was combined with 14.3 mL of deionized water. The resultant solution was raised to 75 °C and stirred for 15 min. Next, 0.8 mL of freshly prepared 10% aqueous triethylamine (TEA) was added and allowed to stir for 15 minutes. 1.5 mL of the silica precursor tetraethylorthosilicate (TEOS, Sigma-Aldrich) was then added at a rate of 0.1 mL min<sup>-1</sup>. To generate MSNs in the range of 60 nm, this reaction was allowed to evolve for 1 h at 80 °C. After 1 h, the reaction was quenched by diluting in EtOH and the particles were washed several times with EtOH *via* centrifugation below 5000 rpm. Prior to the removal of CTAB, particles were resuspended in a volume of deionized water corresponding to 2 mL of H<sub>2</sub>O to 25 mg of MSN for surface functionalization. The pH of the suspension was adjusted with ammonium hydroxide into the range of 8.0–9.0, and the particle solution was pre-annealed at 70 °C. 50  $\mu$ L of [ $N^1$ -(3-trimethoxysilylpropyl) diethylenetriamine]

(Santa Cruz Biotechnology) was added dropwise and allowed to react for 3 hours before the reaction was quenched in ethanol. For CTAB removal, the particles were washed in a MeOH and HCl solution (500 : 19, v/v) for 24 h at room temperature. The particles were collected *via* centrifugation and thoroughly washed in EtOH.

The size of the MSNs was determined by two methods. First, dilute suspensions of MSNs in EtOH were applied to 3 nm carbon film grids (Ted Pella) and allowed to dry. Next, a FEI Tecnai F30 300 keV Transmission Electron Microscope was used to image the particle samples. TEM images of multiple independently synthesized batches were analyzed in ImageJ to calculate a hard sphere diameter for the MSNs. The hydrodynamic diameter and surface charge of the particles were measured *via* dynamic light scattering and electrophoretic light scattering, respectively (90Plus, Brookhaven Instruments).

### 2.2 Loading of STING agonist into nanoparticles

To load STING agonist into the particles, MSNs were washed multiple times in water at a pH of 10.2 *via* repeated sonication and centrifugation. Washed particles were then suspended with cyclic diguanylate monophosphate (cGMP; InvivoGen) in a solution of water at a pH of 10.2 at a ratio of 65  $\mu$ g cGMP per 1 mg MSN, and the suspension was shaken at room temperature for a minimum of 8 hours. Afterwards, the particles were centrifuged out and cGMP loading was measured *via* spectrophotometry measurements of the loading supernatant at a wavelength of 284 nm (Tecan Infinite 200). For stability studies, immuno-MSNs were suspended in PBS at 37 °C (pH of 5.5 or 7.4), and cGMP release was measured across a 20k MWCO mini dialysis unit (Thermo Fisher Scientific) at regular intervals.

### 2.3 PEGylation of immuno-MSN

NH<sub>2</sub>-MSNs were suspended at 10 mg mL<sup>-1</sup> and pH was adjusted to near neutral (7.0–7.5). 2 kDa NHS-PEG-FITC (NANOCS) was dissolved in DMSO and added to the particle suspension at ratios varying from 2 : 1 to 200 : 1 (wt/wt). The suspension was reacted on a shaker for 2 h at room temperature. Once the reaction was complete, the reaction supernatant was collected, and absorption was read at 494 nm (Tecan Infinite 200) to measure the amount of PEG-FITC reacted to the surface of the MSN. For flow cytometry experiments, 2 kDa mPEG-NHS succinic acid (NANOCS) was used in place of FITC-PEG-NHS. The zeta potential of each particle formulation was measured (90Plus, Brookhaven Instruments) to ensure a positive surface charge had been retained.

### 2.4 Analysis of immuno-MSN efficacy *in vitro*

To measure the buffering capacity of the amine-functionalized MSNs, the particles were suspended in a deionized water and NH<sub>4</sub>OH was added dropwise to achieve a pH above 9. Next, 1 M HCl was added in 1  $\mu$ L increments and the subsequent pH of the solution was recorded. The buffering capacity was then calculated as the change in pH per  $\mu$ L of 1 M HCl added.

Next, the intracellular distribution of particles as a function of time was qualitatively investigated. To visualize particles, NH<sub>2</sub>-MSNs were reacted with an Alexa 546 NHS dye (200 : 1, wt/



wt) in deionized water for 2 hours. RAW 264.7 macrophages (300 000 cells per mL) were allowed to adhere to a glass bottom cell culture dish for 24 hours before they were treated with the AF647-MSNs at 0.72 mg MSN per mL. Samples were collected 2 and 6 h following treatment, rapidly washed with PBS, fixed with 2% PFA in PBS for 30 minutes, and then mounted onto a glass slide with DAPI mounting medium (Vector Laboratories) and No. 1.5 glass cover slips. Confocal images of the particles and cells were captured with a TCS SP8 gated STED confocal microscope (Leica Microsystems).

To determine that enhanced intracellular distribution of the immuno-MSN corresponded to increased therapeutic efficacy, the IFN- $\beta$  production of RAW 2647 macrophages exposed to CDN-MSNs and free CDN was compared. 6 million RAW 2647 macrophages were co-plated in 1.5 mL of cell media with treatments of 30  $\mu$ g of free CDN and MSN-loaded CDN. After 24 h, the media was spun, and the supernatant collected. IFN- $\beta$  production was measured following the manufacturer's protocol using a LumiKine Xpress Bioluminescent Cytokine ELISA Kits (InvivoGen) and luminescence readings were obtained with the Tecan Infinite 200 spectrophotometer.

### 2.5 Effect of serum proteins on the uptake of immuno-MSN by splenocytes *ex vivo*

Fluorescently-labeled immuno-MSNs were added to DMEM culture media with 10% fetal bovine serum (FBS) to a final concentration of 1 mg mL<sup>-1</sup>. The immuno-MSNs were incubated in the serum media at 37 °C for 24 h and were collected and used in subsequent studies. Identical conditions were used for the bare, light-PEG and dense-PEG immuno-MSN variants. Spleens from healthy BALBc/J mice were harvested, homogenized and passed through 70  $\mu$ m filters. Any residual red blood cells were eliminated using an ACK lysis buffer. Splenocytes (6  $\times$  10<sup>6</sup> cells) were plated in 24-well plates in serum free DMEM media. The serum-incubated immuno-MSNs were added to the splenocytes at a concentration of 20  $\mu$ g mL<sup>-1</sup> CDN (STING agonist) and kept for 24 h at 37 °C. The supernatant was collected for quantification of IFN- $\beta$  secretion using ELISA. The splenocytes were then harvested, resuspended in 600  $\mu$ L of media and analyzed *via* flow cytometry.

### 2.6 Institutional animal care and use committee statement

All animal procedures were conducted under protocols approved by the Institutional Animal Care and Use Committee (IACUC) of Case Western Reserve University (CWRU). CWRU follows the Guide for the Care and Use of Laboratory Animals, which is required by the United States Public Health Service Policy (PHS) on humane care and use of laboratory animals.

### 2.7 Cells and animal models

Metastatic murine 4T1 breast adenocarcinoma cells expressing green fluorescent protein and luciferase (gifted from the William Schieman Lab at Case Western Reserve University) and murine RAW 264.7 macrophages (ATCC) were cultured in DMEM (Gibco) containing 10% FBS (Hyclone) and 1% penicillin-streptomycin (Sigma-Aldrich). Short tandem repeat

analysis was used to validate all cell lines and regular testing was performed for mycoplasma contamination. Cells were cultured at 37 °C and 5% CO<sub>2</sub>.

To generate an orthotopic 4T1 model, female C57BL/6 albino mice (Jackson Laboratories) between 8–10 weeks were anesthetized, shaved, and a 1–2 mm incision was made in the lower left abdomen. 4T1 cells (5  $\times$  10<sup>5</sup>) were orthotopically injected into the mammary fat pad. After inoculation, mice were monitored daily until a palpable tumor was confirmed, at which point tumor progression was monitored *via* tumor caliper measurements (longest axis and perpendicular width) and bioluminescent imaging (IVIS Spectrum, Perkin Elmer) 10 minutes after intraperitoneal injection of 200  $\mu$ L of D-luciferin at 12.5 mg mL<sup>-1</sup>. In all *in vivo* studies, mice were treated with their first particle dose on day 8, and in treatment studies this was followed with a second treatment on day 9.

### 2.8 Biodistribution and cell uptake of immuno-MSN *in vivo*

DAPI, CD45 (30-F11), CD3e (145-2C11), CD11b (M1/70), CD11c (HL3), CD19 (1D3), CD49b (DX5), and F4/80 (T45-2342) dye-conjugated flow cytometry antibodies were purchased from BD Biosciences. Anti-mouse CD4 (GK1.5), CD8a (53-6.7), CD25 (3C7), CD80 (16-10A1), CD206 (C068C2), Ly-6C (HK1.5), and Ly-6G (1A8) antibodies were purchased from Biolegend.

To analyze biodistribution, AlexaFluor 750 NHS (Thermo Fisher Scientific) was reacted with densely PEGylated, lightly PEGylated, and bare NH<sub>2</sub>-MSNs for 2 h in deionized water at room temperature (100 : 2.15, wt/wt). Three groups of mice ( $n$  = 5 per group) were orthotopically inoculated with metastatic 4T1 mammary fat pad tumors. On day 8, each group received a single tail vein injection of 0.2 mg of the different MSN formulations, and 24 h later the mice were sacrificed, and their spleen, lungs, tumor, and blood collected for FACS analysis. The tumor and lungs were digested in collagenase solution (1 mg mL<sup>-1</sup>, Sigma-Aldrich) before all organs were homogenized and passed through 70  $\mu$ m filters. ACK lysis buffer was used to eliminate any remaining red blood cells in the blood and organ cell suspensions. After staining and fixing, cells were read on a BD FACS LSR II Flow Cytometer (Becton Dickinson) and then analyzed with FlowJo software. In total, dendritic cells (CD45<sup>+</sup>-CD11c<sup>+</sup>), natural killer cells (CD45<sup>+</sup>-CD49b<sup>+</sup>), M1 macrophages/M2 macrophages (CD45<sup>+</sup>/CD11b<sup>+</sup>-F4/80<sup>+</sup>-CD80<sup>+</sup>/CD206<sup>+</sup>), general immune cells (CD45<sup>+</sup>), and—in the blood—neutrophils (CD45<sup>+</sup>-CD11b<sup>+</sup>-Ly6G<sup>+</sup>-Ly6C<sup>-</sup>) were analyzed.

For treatment studies, lightly and densely PEGylated NH<sub>2</sub>-MSNs were synthesized and loaded with 50  $\mu$ g CDN per mg MSN. Three groups of  $n$  = 5 mice were inoculated with orthotopic 4T1 tumors and separated into two treatment groups and an untreated control. On days 8 and 9, the treatment groups received a tail vein injection of either the light or dense CDN-MSN formulation containing 10  $\mu$ g of CDN. On day 11 organs were collected and FACS analysis was performed.

### 2.9 Statistical analysis

Prism 8 software was used for statistical analysis (GraphPad). The statistical methods used included unpaired *t*-test (two



tailed) and one-way ANOVA with Kramer–Tukey *post hoc* analysis. All statistical significances reported are for *p* values of less than 0.05. All groups used in this study included a minimum of 3 biological replicates or, for animal studies, at least 5 mice.

### 3. Results and discussion

#### 3.1. Synthesis of immuno-MSN nanoparticles

Tetraethylorthosilicate (TEOS) underwent a controlled condensation reaction in the presence of a regular hexagonal CTAB scaffold (Fig. 1A). Removal of CTAB produced a ‘bare’ MSN that DLS measurements showed to be monodisperse with a hydrodynamic diameter in the range of 80–100 nm (Fig. 1B). TEM images showed uniform mesoporous spheres with a diameter of  $61 \pm 6$  nm (Fig. 1C). In order to create a particle with the ability to tightly bind and sequester CDN from systemic clearance and degradation, the MSN particles reacted with  $N^1$ -(3-trimethoxysilylpropyl)diethylenetriamine, adding positive diethylenetriamine groups to the surface of the particle that form strong ionic bonds with the phosphonate backbone of CDN molecules. Zeta potential measurements of the MSNs before and after the amine-functionalization supported the addition of positive functional groups, with zeta potential of the particles rising from an initial value of  $-4 \pm 6$  to  $44 \pm 2$  mV (Fig. 1D). Then, the ability to load CDN into MSNs was measured. A suspension of amine-functionalized MSNs was allowed to react with CDN overnight. Successful loading of CDN into MSNs should neutralize the positive amines of the particle. This was

confirmed by the zeta potential decreasing to a near-neutral value following loading (Fig. 1D). Overall, the loading consistency and efficiency were very high with nearly 100% of the added amount of CDN being loaded into MSNs, resulting in 50  $\mu\text{g}$  CDN per mg of MSN (Fig. 1E).

#### 3.2. Synthesis of immuno-MSNs with different degree of PEGylation

To optimize the delivery of immuno-MSN to innate immune cells with the tumor microenvironment, the impact of the PEG conformation on the MSN particle was investigated. In particular, it was necessary to investigate particles coated with light or dense PEG resulting in a mushroom or a brush conformation, respectively. For the 2 kDa mPEG used in this study, PEG exists in the mushroom conformation below 0.027 PEG molecules per  $\text{nm}^2$ .<sup>29</sup> To create MSN formulations with these specific surface densities of PEG, varying amounts of NHS-PEG-FITC was reacted with amine-functionalized MSN. After the reaction, the particles were isolated *via* centrifugation and the absorbance of the supernatant at 494 nm was used to determine the amount of PEG-FITC conjugated on the MSN particles. Fig. 2A and B shows the size of the bare, light-PEG and dense-PEG MSN formulations (as measured by DLS) and the degree of PEGylation for each formulation. We examined the effect of PEGylation (and its consumption of surface amines) on CDN loading. Even though the inner porous structure of the MSN is the major contribution to loading, we concluded that

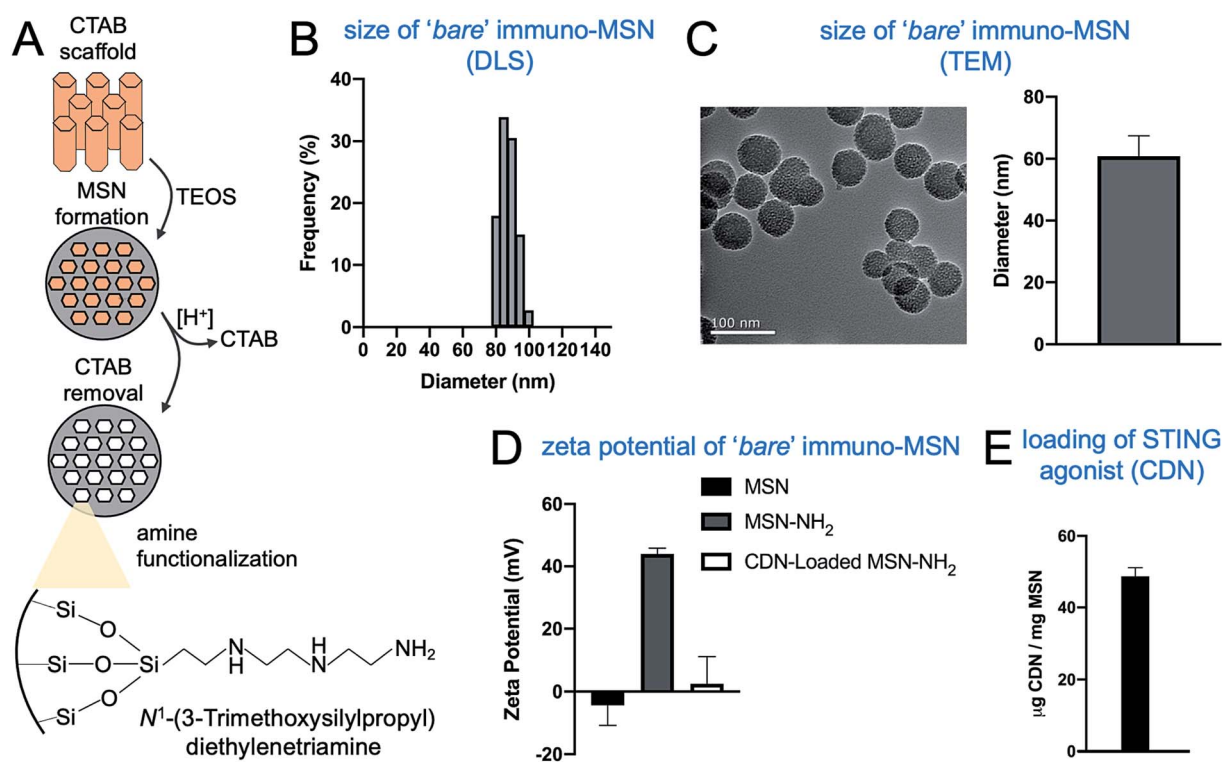


Fig. 1 Synthesis of immuno-MSN. (A) Schematic shows the synthesis of the amine-functionalized MSN. (B) The hydrodynamic size of MSNs was measured using dynamic light scattering. (C) TEM was used to characterize the structure and size of the MSNs. (D) The zeta potential of MSNs was measured before and after amine functionalization and after CDN loading. (E) Loading of MSN was highly consistent and efficient.





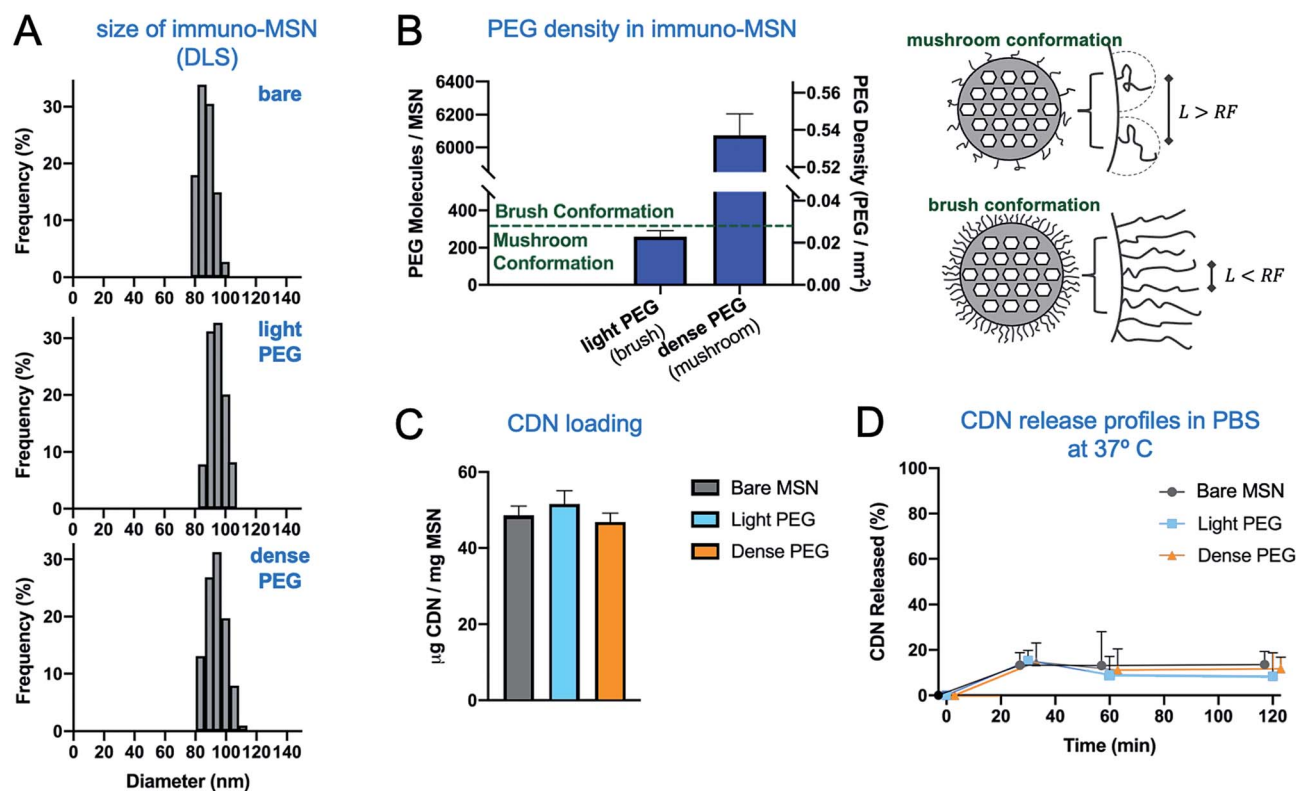


Fig. 2 Characterization of immuno-MSN variants with different PEGylation *in vitro*. (A) The hydrodynamic size of the immuno-MSN variants was measured using dynamic light scattering. (B) Using fluorescent analysis, the number of PEG molecules per MSN particle was measured. (C) The CDN cargo of the immuno-MSN variants is shown. (D) Release of CDN from the immuno-MSN variants was evaluated at 37 °C.

PEGylation was limiting the loading capacity compared to the bare MSN. To achieve consistent loading across all three formulations, we loaded all three formulations based on the formulation with the lowest loading capacity, dense-PEG MSN. As shown in Fig. 2C, CDN loading for the two PEGylated MSN (light and dense PEG) was determined to be consistent with the bare MSN. The release profiles in PBS indicate that all the formulations were stably loaded with CDN (Fig. 2D). It has been shown that the density of PEG molecules on the surface of a nanoparticle influences their molecular conformation and, subsequently, their immunoevasion capability.<sup>26–28</sup> At low densities, PEG molecules take on a mushroom conformation where molecules are free to move independent of one another and effectively fill a hemisphere of space corresponding to the particle's Flory radius; meanwhile at high densities, PEG molecules restrict one another to exist in a more radially outward configuration. The specific conformation of surface PEG has been shown to influence the deposition of nanoparticles into tumors.<sup>28,30</sup>

### 3.3. Evaluation of the immuno-MSN efficacy *in vitro*

In addition to loading CDN, diethylenetriamine gives the MSN its high number of amines, which provides a strong buffering effect. With an adequately high buffering capacity, particles internalized *via* endocytosis can manipulate the endosomal

acidification process to create a strong osmotic gradient that drives water into the endosome leading to the escape of the MSN particle. This mechanism, referred to as the proton sponge effect, enables MSN to deliver CDN into the cytoplasm, where it must be presented to stimulate the STING pathway. To determine whether the buffering effect of the MSN particles was in the appropriate pH range, we used titrations to measure the buffering capacity of the particles and normalized this value per particle. We compared the buffering capacity of MSN to the established cationic polymer polyethyleneimine (PEI) with MW of 25 kDa, which is known to cause the proton sponge effect.<sup>31</sup> In the physiologically relevant pH range of 7.4–5.5, we observed that the amine-functionalized MSNs produced at least an order of magnitude greater buffering capacity than PEI (Fig. 3A). Next, to evaluate whether the high buffering capacity of MSNs results in endosomal escape, confocal images of the intracellular distribution of MSNs were captured as a function of time. MSNs were fluorescently labeled and incubated with macrophages, with cells collected, fixed, and stained with DAPI at 2 and 6 hours. While the images at 2 hours showed fluorescent particles were almost exclusively confined to punctate intracellular compartments, images at 6 hours showed fluorescent particles had become diffuse within the cell (Fig. 3B). In a recent study,<sup>19</sup> we showed that mild acidification from pH 7.4 to pH 5.5 (mimicking late endosomal conditions) caused a 4-fold increase of CDN release from MSNs. Finally, the ability of immuno-MSN



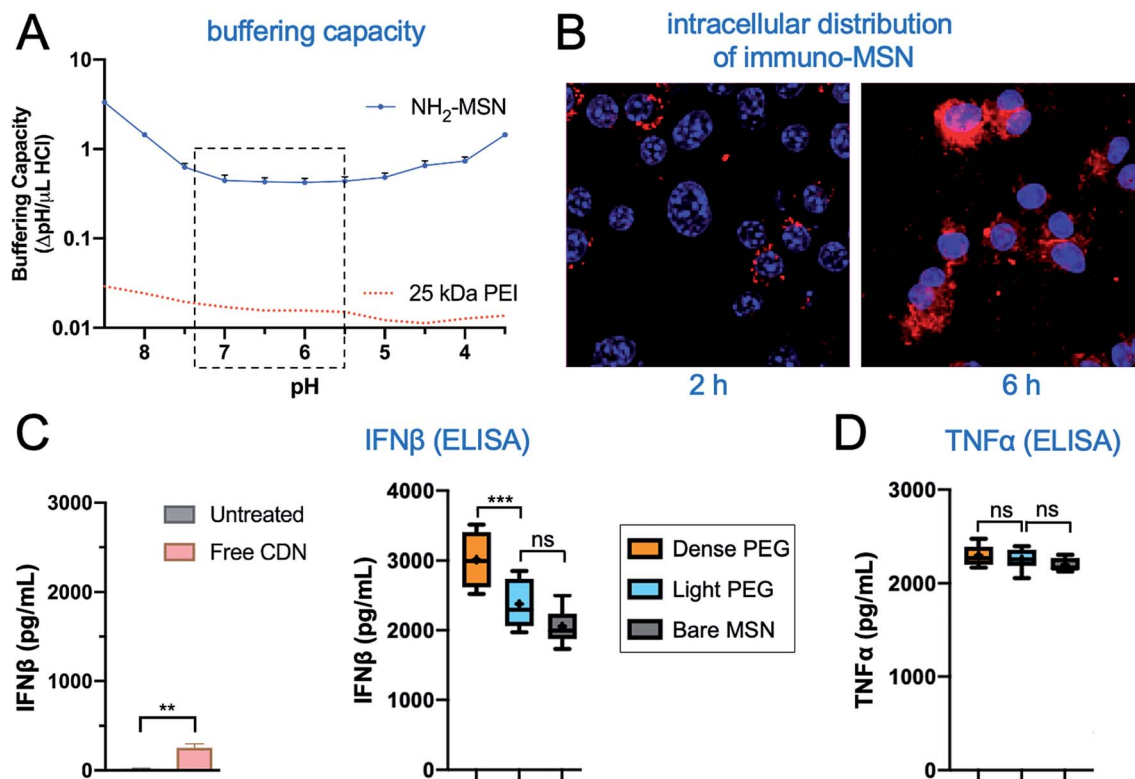


Fig. 3 Evaluation of the efficacy of immuno-MSN *in vitro*. (A) Proton buffering of the immuno-NP based on titration curves ( $n = 3$ ). The curve of PEI (red dotted line) was extracted from ref. 31. (B) Confocal microscopy monitored the intracellular distribution of fluorescently labeled immuno-MSN as a function of time. ELISA analysis measured the *in vitro* production of (C) IFN- $\beta$  and (D) TNF $\alpha$  from RAW 264.7 macrophages 24 h after co-incubation with free CDN or immuno-MSN. All conditions were performed in triplicate and plotted as mean  $\pm$  standard error with statistics by one-way ANOVA with Tukey's/Sidak's post-test ( $P$  values: \*\*  $< 0.01$ , \*\*\*\*  $P < 0.0001$ ).

to proficiently deliver CDN into APCs was evaluated by measuring IFN- $\beta$  and TNF $\alpha$  production. Macrophages were incubated with equivalent doses of free CDN and CDN-loaded

MSNs for 24 h, and IFN- $\beta$  production was measured with an ELISA. The immuno-MSN generated a remarkable 9-fold higher production of IFN- $\beta$  compared to free CDN (Fig. 3C), suggesting

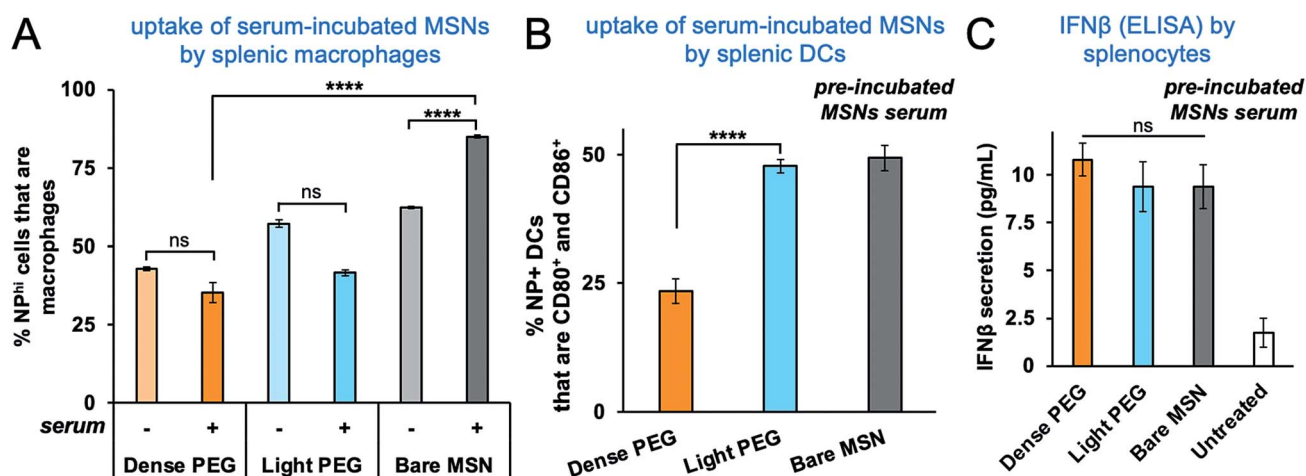


Fig. 4 Evaluation of the PEGylation on the serum protein absorption *ex vivo*. Fluorescently-labeled immuno-MSNs were incubated in a serum-containing media (DMEM media with 10% FBS) at 37 °C for 24 h. The serum-incubated MSNs were added to a cell culture of splenocytes that were harvested from healthy BALBc/J. Splenocytes ( $6 \times 10^6$  cells) and serum-incubated immuno-MSNs ( $20 \mu\text{g mL}^{-1}$  CDN) were kept for 24 h at 37 °C. Identical conditions were used for the bare, light-PEG and dense-PEG immuno-MSN variants. Analysis was performed for uptake by (A) splenic macrophages and (B) splenic DCs using flow cytometry, and (C) secretion of IFN- $\beta$  secretion using ELISA ( $n = 6$ ). Statistical significance was conducted by one-way ANOVA with Sidak's post-test (NS not significant, \*\*\*\*  $P < 0.0001$ ).



that immuno-MSN facilitated intracellular delivery and shuttled CDN out of endosomes and into the cytosol, which allowed direct access to STING. It should be mentioned that 'empty' MSN particles induced negligible production of IFN- $\beta$ .<sup>19</sup> Comparison of IFN- $\beta$  (Fig. 3C; right panel) and TNF $\alpha$  production (Fig. 3D) showed negligible differences between the 3 MSN variants. The only exception was the significantly higher production of IFN- $\beta$  in the case of the dense-PEG MSN variant.

We then sought to functionally evaluate the effect of PEGylation on the serum protein adsorption. The immuno-MSN variants were incubated in culture media with 10% serum (FBS) at 37 °C for 24 h to allow protein adsorption. The nanoparticles were then washed and added to splenocytes that were harvested from healthy BALBc/J mice. After 24 h of incubation, the uptake of bare immuno-MSN by splenic macrophages was significantly higher when the particles had been pre-incubated with serum (Fig. 4A). As expected, PEGylation provided

a significant level of protection from serum protein absorption as indicated by their lower uptake by macrophages. On the other hand, only the dense-PEG MSN exhibited lower uptake by activated splenic DCs (Fig. 4B), whereas bare and light-PEG MSNs showed similarly high uptake. Most notably, all three formulations generated similar IFN- $\beta$  secretion by splenocytes (Fig. 4C).

It is increasingly apparent that a potent antitumor immune response can play a vital role in the outcome of cancers, with a high density of infiltrating T-cells correlating with improved cancer prognosis.<sup>32</sup> Importantly, advanced tumors contain a high concentration of pro-tumor lymphocytes secreting immunosuppressive cytokines, creating a chemical barrier to systemic T-cell infiltration.<sup>33</sup> Although the clinical potential of these immunotherapies is clear, it also appears increasingly necessary to supplement the T-cell centric therapies with additional immunoadjuvants to assist in remodeling the

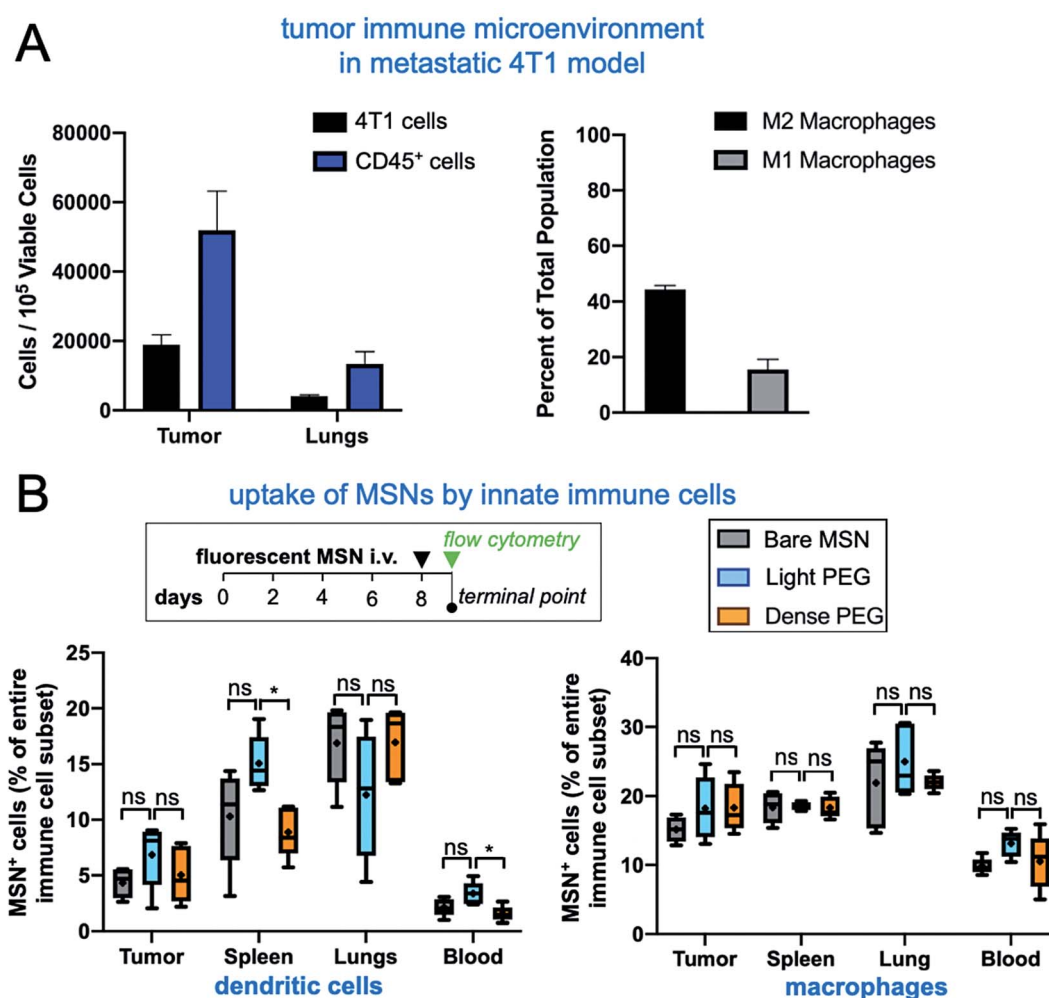


Fig. 5 Evaluation of the microdistribution of immuno-MSN variants with different levels of PEGylation in the tumor immune microenvironment in the orthotopic 4T1 mouse model. (A) Flow cytometry analysis showed the high content of resident immune cells in the microenvironment of primary tumor and lung metastasis (left panel), including high levels of the immunosuppressive phenotype of M2-like macrophages (right panel). Cell count data from flow cytometry analysis was normalized to 10<sup>5</sup> viable cells. (B) The schedule of administration and analysis of systemically injected fluorescently labeled immuno-MSNs are shown at the top. Flow cytometry analysis of the uptake of fluorescently labeled immuno-MSN by DCs (left panel) and macrophages (right panel) in tumor, spleen, lungs and blood is shown ( $n = 5$  mice per group). Statistical significance in the box and whisker plot (5–95 percentile, "+" mean) was conducted by one-way ANOVA with Sidak's post-test (ns not significant, \* $P < 0.05$ ).



immunosuppressive microenvironment of advanced tumors. STING agonists present a new family of highly potent immunostimulatory agents that induce the production of type I interferon and activate the innate immune compartment of tumors, creating a potent, self-perpetuating inflammatory immune response within the tumor microenvironment.<sup>34–36</sup> Being oligonucleotides, STING agonists face several challenges, including crossing the cell membrane. Here, we show that MSN nanoparticles offer great flexibility to not only stably load CDN, but also to equip the particle with chemical properties, such as a strong buffering capacity that can enhance cytoplasmic delivery and subsequent secretion of proinflammatory cytokines. It has been previously shown that particles with a high density of amines with  $pK_a$  in the range of 6–7 can disrupt endosomal acidification and cause endosomal lysis *via* a phenomenon known as the proton sponge effect.<sup>25</sup> As the endosome actively pumps hydrogen ions into the interior of the endosome, the amine groups of the particles adsorb these protons and become positive, generating an electrochemical

gradient that causes small negative ions to flow into the endosome. In turn, the accumulated ions inside the endosome create an osmotic gradient that causes water to flow into the endosome, causing the compartment to swell and lyse, thereby exposing the nanoparticles to the cell cytoplasm. Ethylene triamine is a small molecule with three amines in close proximity, giving these amines a  $pK_a$  in the target range of 6–7.<sup>24</sup> By adding a high density of this molecule in the highly porous MSNs, these nanoparticles are not only able to closely bind CDN as they traffic the drug to the perivascular regions of a tumor, but also have the potential to deliver the STING agonist into the cell cytoplasm where its binding partner is located. In a previous study, we quantitatively assessed the capability of cytosolic delivery of the STING agonist by the immuno-MSN.<sup>19</sup>

### 3.4. Effect of degree of PEGylation on the uptake of immuno-MSN by innate immune cells *in vivo*

To investigate the impact of PEGylation on the microdistribution of the immuno-MSN *in vivo*, we used the orthotopic

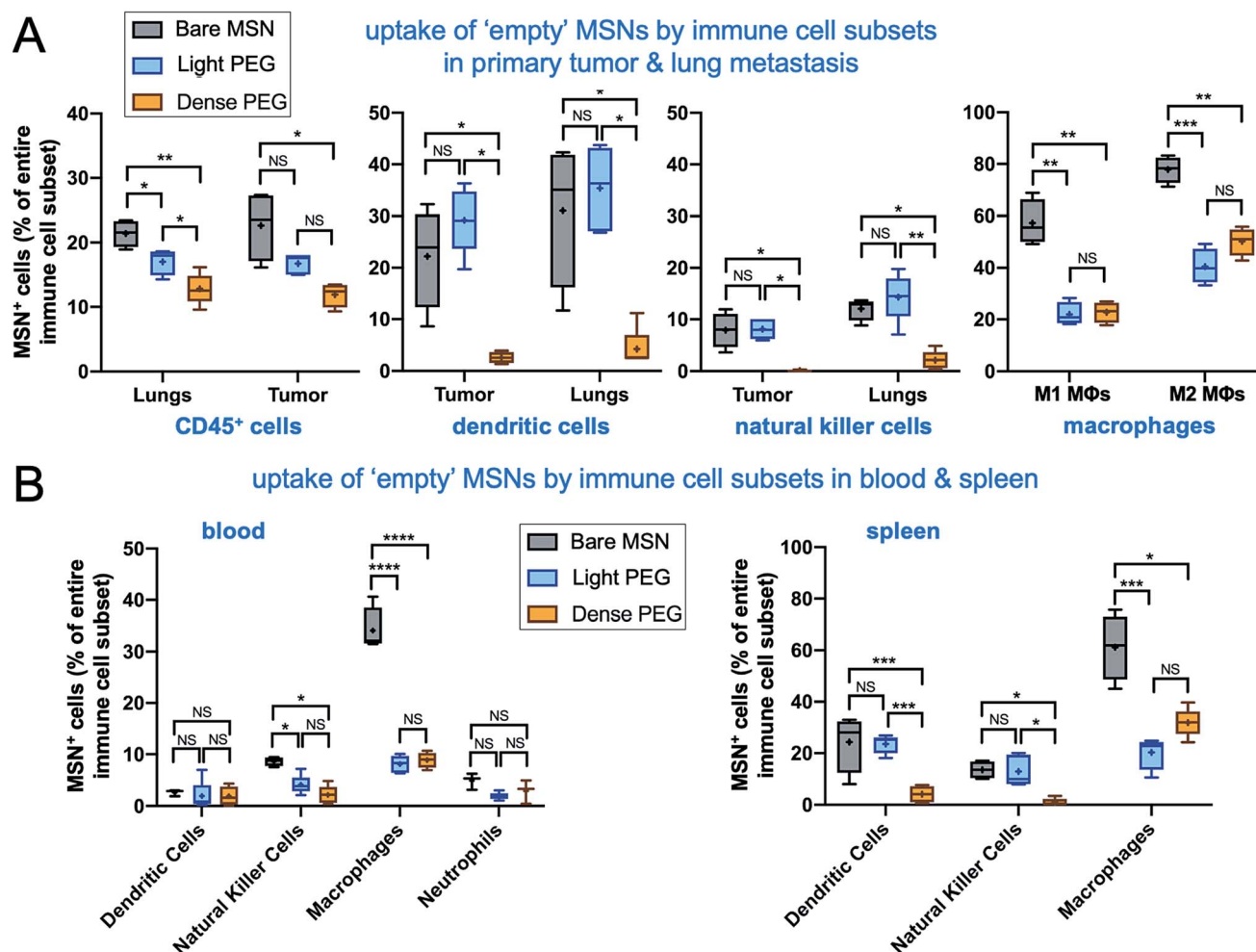


Fig. 6 Evaluation of the microdistribution of 'empty' MSN variants with different levels of PEGylation in the tumor immune microenvironment in the orthotopic 4T1 mouse model. (A) Flow cytometry analysis of the uptake of fluorescently labeled immuno-MSN by immune cells, DCs, NK cells and macrophages in the primary tumor and lung metastasis ( $n = 5$ ). (B) Flow cytometry analysis of cell uptake of fluorescently labeled immuno-MSNs in blood and spleen ( $n = 5$ ). Statistical significance in the box and whisker plot (5–95 percentile, "+" mean) was conducted by one-way ANOVA with Sidak's post-test (NS not significant, \* $P < 0.05$ , \*\* $P < 0.01$ , \*\*\* $P < 0.001$ , \*\*\*\* $P < 0.0001$ ).





4T1 mouse model with the 4T1 cells expressing firefly luciferase and green fluorescent protein (GFP). Tumor progress was monitored using BLI imaging. On day 8 after tumor inoculation, mice were intravenously injected with fluorescently labeled (AlexaFluor 647) bare, light-PEG, or dense-PEG MSN variant at a dose of 10  $\mu\text{g}$  CDN per mouse ( $n = 5$  mice per group). First, flow cytometry analysis of the immune landscape of untreated mice with 4T1 tumors show that the immune cell content in the tumor microenvironment of the primary tumor and lung metastasis is significant, with the number of immune cells being more than two-fold higher than cancer cells (Fig. 5A). Notably, the ratio of M2 over M1 polarized macrophages in the tumor was measured to be 2.75, indicating a highly immunosuppressive microenvironment. Next, tumor, blood, spleen, and lungs were collected 24 h after the immuno-MSN injection for FACS analysis. Innate immune cells were isolated *via* flow cytometry and the fraction of immuno-MSN-AF647<sup>+</sup> cells was measured for DCs (Fig. 5B; left panel) and macrophages (right panel). Notably, there was no significant differences between the uptake of the three immuno-MSN variants by either DCs or macrophages in the tumor and lungs that are colonized by early 4T1 metastasis, indicating that PEGylation had little influence in the uptake of the immuno-MSNs by these professional phagocytes at least at 24 h after systemic administration. Notably, splenic DCs exhibited higher uptake of light-PEG MSN than the dense-PEG variant.

In a separate study, we performed the same study using the 'empty' MSN variants without the CDN cargo. The surface charge of these MSNs was positive rather than neutral for the CDN-loaded MSNs (Fig. 1). In total, dendritic cells, natural killer cells, M1 and M2 macrophages, general immune cells, and

neutrophils were analyzed. In metastatic lungs and tumor, the 'empty bare MSN exhibited the highest overall uptake by immune cells compared to the two PEGylated MSN variants (Fig. 6A). This was especially apparent in the uptake of 'empty' bare MSNs by macrophages (both M1 and M2). A comparison between the two 'empty' PEGylated MSN variants showed that light-PEG formulation had significantly higher uptake by DCs and natural killer (NK) cells in the primary tumor and lungs than the dense-PEG MSN. Unsurprisingly, the bare MSN displayed significantly greater uptake in the reticuloendothelial system, appearing in 61% of macrophages in the spleen (Fig. 6B).

Although the immuno-MSN exhibited efficacy *in vitro*, delivery to the desired innate immune cells in tumors is another hurdle for STING agonists. Although intratumoral delivery of immunoadjuvants offers a tempting solution to the issue of precise and effective delivery to tumors, it is also apparent that direct administration cannot achieve sufficient spread of the agent throughout the tumor volume and reach the majority of the dysfunctional immune cells within tumors. Also, direct intratumoral delivery to sites of micrometastasis is not feasible due to lack of knowledge of the exact location of the spread of the disease. On the other hand, it has been shown that systemically administered silica nanoparticles deposit in the perivascular region of various murine tumor models, providing access to the numerous inactive innate immune cells present in this exact space.<sup>19,22,23,37</sup> Here, we observed that surface charge had a greater effect on the microdistribution and uptake of systemically administered MSNs by tumor-resident innate immune cells than the surface density of PEG itself.

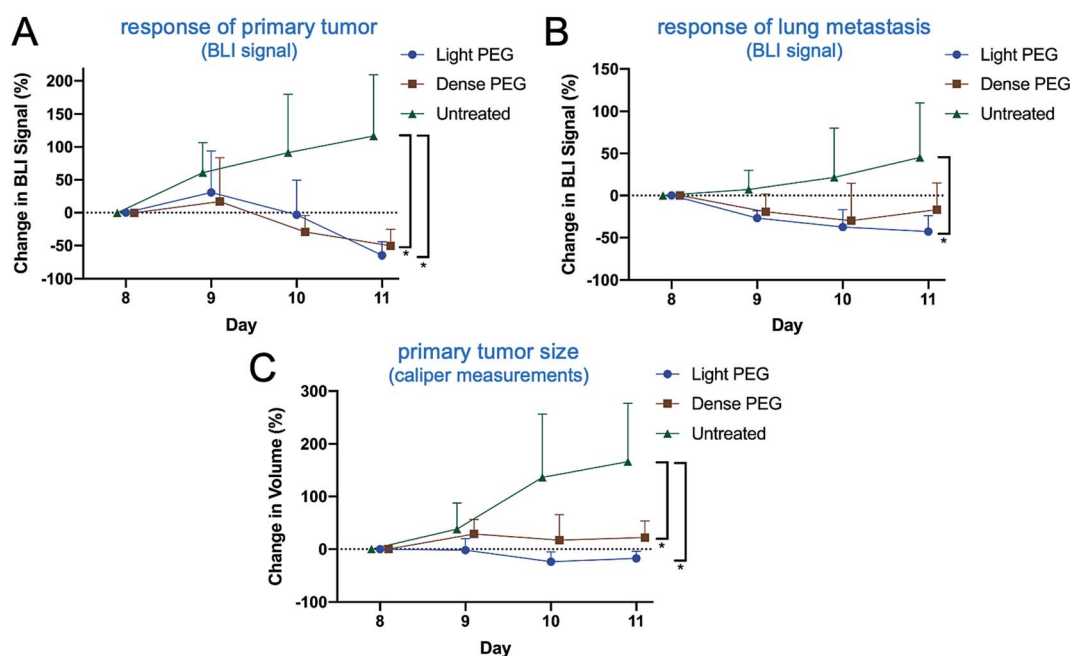


Fig. 7 Evaluation of the efficacy of the immuno-MSN variants in the orthotopic 4T1 mouse model. Mice bearing 4T1 tumors were treated on day 8 and 9 after tumor inoculation. Each dose of immuno-MSN contained 10  $\mu\text{g}$  CDN ( $n = 5$  mice per group). Quantification of longitudinal BLI imaging is shown for (A) primary tumor and (B) lung metastasis. (C) The size of the primary tumor was measured using a caliper.



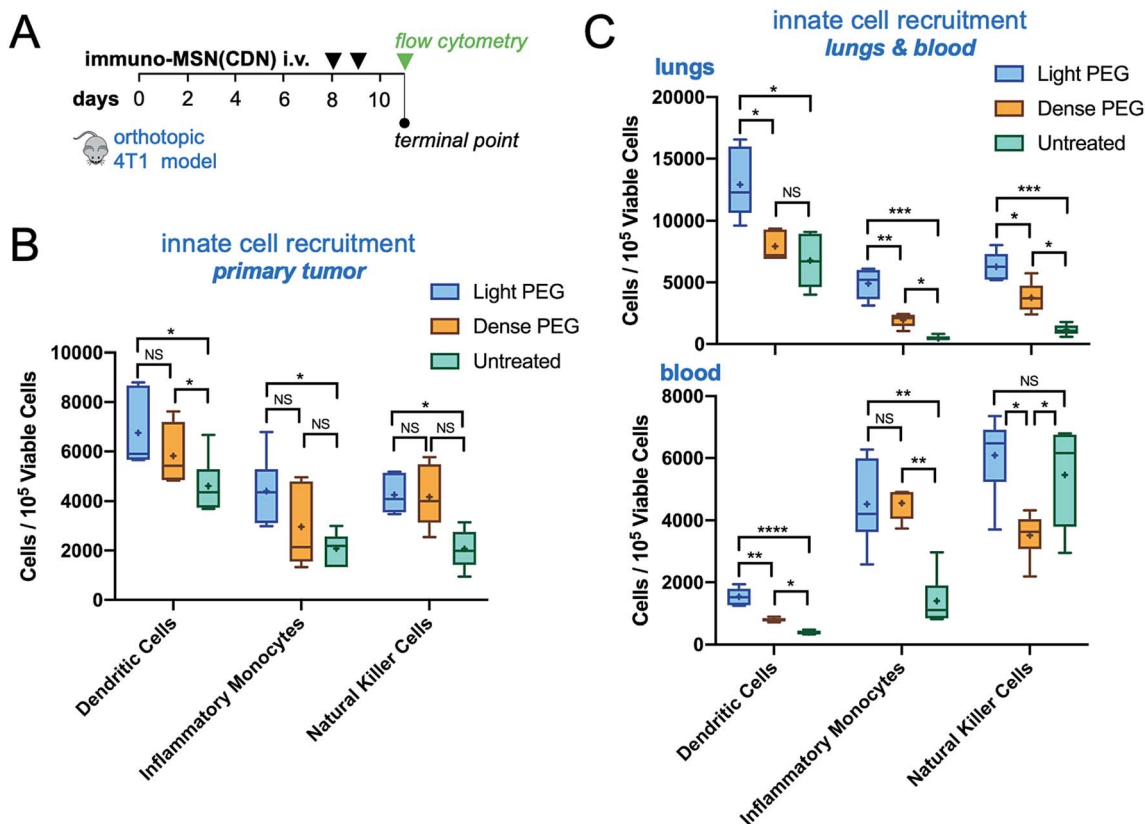


Fig. 8 Quantification of cellular response to the immuno-MSN treatment. (A) Treatment regimen of immuno-MSN variants at a dose of 10  $\mu\text{g}$  CDN per dose ( $n = 5$  mice per group). Flow cytometry analysis of DCs, monocytes and NK cells is shown for (B) the primary tumor and (C) lungs and blood. Statistical significance in the box and whisker plot (5–95 percentile, “+” mean) was conducted by one-way ANOVA with Sidak’s post-test (NS not significant, \* $P < 0.05$ , \*\* $P < 0.01$ , \*\*\* $P < 0.001$ , \*\*\*\* $P < 0.0001$ ). Cell count data from flow cytometry analysis was normalized to  $10^5$  viable cells.

### 3.5. The effect of PEGylation on the efficacy of immuno-MSN to recruit innate immune cells in tumors

To further assess the impact of PEGylation on the efficacy of immuno-MSNs, a mechanistic study of innate immune cell recruitment was performed using the orthotopic 4T1 mouse model. The 4T1 cells stably expressed luciferase, which allowed longitudinal monitoring of the primary tumor and metastatic spread using Bioluminescence Imaging (BLI). Mice were treated with the light-PEG or dense-PEG immuno-MSN at a dose of 10  $\mu\text{g}$  CDN per mouse ( $n = 5$  mice per group) on days 8 and 9 after tumor inoculation. Compared to the untreated control, both PEGylated immuno-MSN formulations significantly reduced the tumor burden as indicated by the decreased BLI signal from the primary tumor and lung metastasis (Fig. 7A and B) and caliper measurements of the primary tumor size (Fig. 7C). Overall, the anticancer outcome was similar for the two treatments.

On day 11 after tumor inoculation, tumor, lungs, and blood were collected for FACS analysis (Fig. 8A). In the primary tumor, both PEG formulations caused a similar and significant expansion of DCs compared to the untreated control (Fig. 8B). A similar trend was observed in lung metastasis with the light-PEG MSN outperforming the dense-PEG variant (Fig. 8C, top panel). Additionally, while both light and dense-PEG

formulations produced similar amounts of inflammatory monocytes in the blood, the light-PEG formulation generated significantly higher circulating dendritic cells (Fig. 8C, bottom panel). Overall, the degree of PEGylation affected the uptake of the MSNs by phagocytes. This was not translated to a significant therapeutic outcome within the short treatment timeframe of our study. However, these results indicate that the light-PEG MSN may be more advantageous, especially due to its higher uptake by DCs, which was confirmed in both ex vivo and in vivo studies.

## 4. Conclusions

This study highlights the challenges and enormous potential of drug delivery for cancer immunotherapy. The inherent complexity of the immune system and its network of signaling pathways can make it challenging to reproducibly elicit a desired immune response. Even minor changes to a drug delivery system can have a significant impact on the balance of immune cells receiving a treatment and the outcome of a therapy. First, we show that mesoporous silica nanoparticles can be engineered to efficiently deliver a STING agonist to innate cells, resulting in a nearly 9-fold increase in efficacy compared to the free STING agonist. Further, it was determined



that the degree of PEGylation influenced the destination of 'empty' MSNs *in vivo*, with the light-PEG MSN variant exhibiting greater uptake into innate immune cells in tumor regions compared to the dense-PEG variant. In the case of the immuno-MSN loaded with CDN, the three immuno-MSN variants exhibited statistically insignificant uptake by innate immune cells. It should be noted that a main difference is the neutral surface charge of the immuno-MSN compared to the positive charge of the 'empty' MSN. However, even though the cellular uptake was similar at 24 h after injection for the three immuno-MSN variants, we observed a significant beneficial effect on the activation and expansion of APCs especially in lung metastasis using the light PEG immuno-MSN variant. In this study, we only assessed the microdistribution and cellular uptake of the MSN variants at a single time point (*i.e.*, 24 h post-injection). We anticipate that antitumor immune responses will be strongly dependent on the different kinetics and rate of uptake of immunostimulatory nanoparticles by the professional phagocytes in the tumor and the reticuloendothelial organs. Future studies will need to include additional time points to extract the kinetics of uptake of nanoparticle variants by the various immune cell subsets in different tumor landscapes (*e.g.*, primary or metastatic sites). Overall, the trends observed in this study indicate that subtle factors such as the degree of PEGylation or the surface charge of an immunostimulatory nanoparticle can dramatically alter the efficacy of immunotherapies.

## Conflicts of interest

There are no conflicts to declare.

## Acknowledgements

This work was supported by grants from the National Cancer Institute (R01CA253627, U01CA198892 to E. K.), the Case Comprehensive Cancer Center Support Grant (P30CA043703) and the Shiverick Family Fund (E. K.), and the Clinical Translational Science Collaborative of Cleveland (UL1TR002548 to E. K.). P. B. was supported by the NSF graduate research fellowships program. M. L. and T. J. M. was supported by a fellowship from the NIH Interdisciplinary Biomedical Imaging Training Program (T32EB007509) administered by the Department of Biomedical Engineering, Case Western Reserve University. We acknowledge the Case Center for Imaging Research, Case Comprehensive Cancer Center Flow Cytometry Core, and the Case School of Medicine Light Microscopy Core.

## References

- 1 S. Ma, X. Li, X. Wang, L. Cheng, Z. Li, C. Zhang, Z. Ye and Q. Qian, *Int. J. Biol. Sci.*, 2019, **15**, 2548–2560.
- 2 P. Darvin, S. M. Toor, V. Sasidharan Nair and E. Elkord, *Exp. Mol. Med.*, 2018, **50**, 1–11.
- 3 K. Esfahani, L. Roudaia, N. Buhlaiga, S. V. Del Rincon, N. Papneja and W. H. Miller Jr, *Curr. Oncol.*, 2020, **27**, S87–S97.
- 4 P. Bonaventura, T. Shekarian, V. Alcazer, J. Valladeau-Guilemond, S. Valsesia-Wittmann, S. Amigorena, C. Caux and S. Depil, *Front. Immunol.*, 2019, **10**, 168.
- 5 G. L. Beatty and W. L. Gladney, *Clin. Cancer Res.*, 2015, **21**, 687–692.
- 6 A. Gardner and B. Ruffell, *Trends Immunol.*, 2016, **37**, 855–865.
- 7 C. E. Lewis, A. S. Harney and J. W. Pollard, *Cancer Cell*, 2016, **30**, 365.
- 8 S. K. Larsen, Y. Gao and P. H. Basse, *Crit. Rev. Oncog.*, 2014, **19**, 91–105.
- 9 J. A. Joyce and D. T. Fearon, *Science*, 2015, **348**, 74–80.
- 10 L. Muller, P. Aigner and D. Stoiber, *Front. Immunol.*, 2017, **8**, 304.
- 11 M. A. Swartz, S. Hirose and J. A. Hubbell, *Sci. Transl. Med.*, 2012, **4**, 148rv149.
- 12 P. U. Atukorale, S. P. Raghunathan, V. Raguveery, C. Zheng, T. J. Moon, M. L. Weiss, P. A. Bielecki, A. L. Goldberg, G. Covarrubias, C. J. Hoimes and E. Karathanasis, *Cancer Res.*, 2019, **79**, 5394–5406.
- 13 T. Su, Y. Zhang, K. Valerie, X. Y. Wang, S. Lin and G. Zhu, *Theranostics*, 2019, **9**, 7759–7771.
- 14 G. N. Barber, *Nat. Rev. Immunol.*, 2015, **15**, 760–770.
- 15 R. S. Riley, C. H. June, R. Langer and M. J. Mitchell, *Nat. Rev. Drug Discovery*, 2019, **18**, 175–196.
- 16 M. S. Goldberg, *Nat. Rev. Cancer*, 2019, **19**, 587–602.
- 17 D. Shae, K. W. Becker, P. Christov, D. S. Yun, A. K. R. Lytton-Jean, S. Sevimli, M. Ascano, M. Kelley, D. B. Johnson, J. M. Balko and J. T. Wilson, *Nat. Nanotechnol.*, 2019, **14**, 269–278.
- 18 N. Cheng, R. Watkins-Schulz, R. D. Junkins, C. N. David, B. M. Johnson, S. A. Montgomery, K. J. Peine, D. B. Darr, H. Yuan, K. P. McKinnon, Q. Liu, L. Miao, L. Huang, E. M. Bachelder, K. M. Ainslie and J. P. Ting, *JCI Insight*, 2018, **3**, e120638.
- 19 P. A. Bielecki, M. E. Lorkowski, W. M. Becicka, P. U. Atukorale, T. J. Moon, Y. Zhang, M. Wiese, G. Covarrubias, S. Ravichandran and E. Karathanasis, *Nanoscale Horiz.*, 2021, **6**, 156–167.
- 20 M. E. Lorkowski, P. U. Atukorale, P. A. Bielecki, K. H. Tong, G. Covarrubias, Y. Zhang, G. Loutrianakis, T. J. Moon, A. R. Santulli, W. M. Becicka and E. Karathanasis, *J. Controlled Release*, 2021, **330**, 1095–1105.
- 21 P. U. Atukorale, S. P. Raghunathan, V. Raguveer, T. J. Moon, C. Zheng, P. A. Bielecki, M. L. Wiese, A. L. Goldberg, G. Covarrubias, C. J. Hoimes and E. Karathanasis, *Cancer Res.*, 2019, **79**, 5394–5406.
- 22 O. Turan, P. Bielecki, V. Perera, M. Lorkowski, G. Covarrubias, K. Tong, A. Yun, G. Loutrianakis, S. Raghunathan, Y. Park, T. Moon, S. Cooley, D. Dixit, M. A. Griswold, K. B. Ghaghada, P. M. Peiris, J. N. Rich and E. Karathanasis, *Adv. Ther.*, 2019, **2**, 1900118.
- 23 O. Turan, P. Bielecki, V. Perera, M. Lorkowski, G. Covarrubias, K. Tong, A. Yun, A. Rahmy, T. Ouyang, S. Raghunathan, R. Gopalakrishnan, M. A. Griswold, K. B. Ghaghada, P. M. Peiris and E. Karathanasis, *Nanoscale*, 2019, **11**, 11910–11921.



- 24 K. A. Curtis, D. Miller, P. Millard, S. Basu, F. Horkay and P. L. Chandran, *PLoS One*, 2016, **11**, e0158147.
- 25 M. Wojnilowicz, A. Glab, A. Bertucci, F. Caruso and F. Cavaliere, *ACS Nano*, 2019, **13**, 187–202.
- 26 A. Gabizon, H. Shmeeda and Y. Barenholz, *Clin. Pharmacokinet.*, 2003, **42**, 419–436.
- 27 A. A. Gabizon, *Cancer Invest.*, 2001, **19**, 424–436.
- 28 R. Gref, M. Luck, P. Quellec, M. Marchand, E. Dellacherie, S. Harnisch, T. Blunk and R. H. Muller, *Colloids Surf., B*, 2000, **18**, 301–313.
- 29 C. Cruje and D. B. Chithrani, *J. Nanomed. Res.*, 2014, **1**, 00006.
- 30 J. L. Perry, K. G. Reuter, M. P. Kai, K. P. Herlihy, S. W. Jones, J. C. Luft, M. Napier, J. E. Bear and J. M. DeSimone, *Nano Lett.*, 2012, **12**, 5304–5310.
- 31 R. V. Benjaminsen, M. A. Matthebjerg, J. R. Henriksen, S. M. Moghimi and T. L. Andresen, *Mol. Ther.*, 2013, **21**, 149–157.
- 32 F. Pages, B. Mlecnik, F. Marliot, G. Bindea, F. S. Ou, C. Bifulco, A. Lugli, I. Zlobec, T. T. Rau, M. D. Berger, I. D. Nagtegaal, E. Vink-Borger, A. Hartmann, C. Geppert, J. Kolwelter, S. Merkel, R. Grutzmann, M. Van den Eynde, A. Jouret-Mourin, A. Kartheuser, D. Leonard, C. Remue, J. Y. Wang, P. Bavi, M. H. A. Roehrl, P. S. Ohashi, L. T. Nguyen, S. Han, H. L. MacGregor, S. Hafezi-Bakhtiari, B. G. Wouters, G. V. Masucci, E. K. Andersson, E. Zavadova, M. Vocka, J. Spacek, L. Petruzella, B. Konopasek, P. Dunder, H. Skalova, K. Nemejcova, G. Botti, F. Tatangelo, P. Delrio, G. Ciliberto, M. Maio, L. Laghi, F. Grizzi, T. Fredriksen, B. Buttard, M. Angelova, A. Vasaturo, P. Maby, S. E. Church, H. K. Angell, L. Lafontaine, D. Bruni, C. El Sissy, N. Haicheur, A. Kirilovsky, A. Berger, C. Lagorce, J. P. Meyers, C. Paustian, Z. Feng, C. Ballesteros-Merino, J. Dijkstra, C. van de Water, S. van Lent-van Vliet, N. Knijn, A. M. Musina, D. V. Scripcariu, B. Popivanova, M. Xu, T. Fujita, S. Hazama, N. Suzuki, H. Nagano, K. Okuno, T. Torigoe, N. Sato, T. Furuhashi, I. Takemasa, K. Itoh, P. S. Patel, H. H. Vora, B. Shah, J. B. Patel, K. N. Rajvik, S. J. Pandya, S. N. Shukla, Y. Wang, G. Zhang, Y. Kawakami, F. M. Marincola, P. A. Ascierto, D. J. Sargent, B. A. Fox and J. Galon, *Lancet*, 2018, **391**, 2128–2139.
- 33 S. J. Bagley and D. M. O'Rourke, *Pharmacol. Ther.*, 2020, **205**, 107419.
- 34 P. Fitzgerald-Bocarsly and D. Feng, *Biochimie*, 2007, **89**, 843–855.
- 35 A. Marcus, A. J. Mao, M. Lensink-Vasan, L. Wang, R. E. Vance and D. H. Raulet, *Immunity*, 2018, **49**, 754–763.
- 36 D. P. Simmons, P. A. Wearsch, D. H. Canaday, H. J. Meyerson, Y. C. Liu, Y. Wang, W. H. Boom and C. V. Harding, *J. Immunol.*, 2012, **188**, 3116–3126.
- 37 O. Turan, P. Bielecki, K. Tong, G. Covarrubias, T. Moon, A. Rahmy, S. Cooley, Y. Park, P. M. Peiris, K. B. Ghaghada and E. Karathanasis, *Mol. Pharm.*, 2019, **16**, 4352–4360.

